HIV-1 uses dynamic capsid pores to import nucleotides and fuel encapsidated DNA synthesis

David A. Jacques[1], **William A. McEwan**[1], **Laura Hilditch**[2], **Amanda J. Price**[1,†], **Greg J. Towers**[2], and **Leo C. James**[1]

[1]MRC Laboratory of Molecular Biology, Francis Crick Avenue, Cambridge Biomedical Campus, Cambridge, CB2 0QH, UK

[2]Infection and Immunity, University College London, Cruciform Building 3.3, 90 Gower Street, London, WC1E 6BT, UK

Abstract

During the early stages of infection, the HIV-1 capsid protects viral components from cytosolic sensors, such as cGAS, and nucleases, such as TREX, while allowing access to nucleotides for efficient reverse transcription1. Here we show that each capsid hexamer has a size-selective pore bounded by a ring of six arginine residues and a 'molecular iris' formed by the N-terminal β-hairpin. The arginine ring creates a strongly positively charged channel that recruits the four nucleotides with on-rates that near diffusion limits. Progressive removal of pore arginines results in a dose-dependent and concomitant decrease in nucleotide affinity, reverse transcription and infectivity. This positively charged channel is universally conserved in lentiviral capsids despite the fact that it is strongly destabilising without nucleotides to counteract charge repulsion. We also describe a channel inhibitor, hexacarboxybenzene, which competes for nucleotide binding and efficiently blocks encapsidated reverse transcription demonstrating the tractability of the pore as a novel drug target.

There is increasing evidence that the HIV-1 capsid remains intact as it traverses the cytoplasm of a newly-infected cell. Prematurely-uncoated viruses trigger innate immune sensing2, assembled capsid proteins are required to properly engage the nuclear pore complex3, and intact capsids have been observed at the nuclear envelope4. Reverse transcription has been postulated to occur within the HIV-1 virion during cytoplasmic

---

transit, yet structural analyses of the HIV-1 capsid have not defined a pore through which small molecules such as dNTP's might pass. One possible location for a pore would be the 6-fold axis at the centre of each capsid protein (CA) hexamer, but this is not evident from existing hexamer structures as it is obscured by the N-terminal β-hairpin. By comparing all the available CA crystal structures with resolved β-hairpins[5–11], including monomeric crystal forms, we observed that the β-hairpin can adopt alternate conformations that differ by up to 15 Å (as measured by the displacement of Q7) (Fig. 1a). When reconstructed in the context of a hexamer, several of these β-hairpin conformations result in a pore about the six-fold axis (Fig. 1b). The different β-hairpin conformations are the result of a pivoting movement of up to 37.5° about the N-terminal proline, an essential capsid residue that forms a salt-bridge with D51[12] (Fig. 1a, Supplementary Video 1). In structures where the pore would be open, D51 also participates in a second salt-bridge interaction with H12. Conversely, in structures where the pore would be closed, including all previously solved disulfide-stabilised hexamers (CA$_{Hexamer}$), a water molecule has displaced the H12 side-chain and coordinates a tetrahedral hydrogen-bond network between H12, T48, Q50 and D51. We hypothesized that the protonation state of H12 may be crucial in determining which arrangement is favored and therefore that the conformation of the β-hairpin in published structures will have been influenced by the pH at which they were solved. Remarkably, when the relative displacement of the β-hairpin (Q7 Cα) is plotted against crystallization pH the structures resolve into two groups; at pH < 7 an open pore β-hairpin conformation is observed whereas at pH > 7 a closed pore conformation is favored (Fig. 1c, Extended Data Table 1). The same correlation is observed when the distance between D51 and H12 is plotted against pH (Fig. 1d,e), confirming the importance of H12 in determining β-hairpin conformation. Structures solved at pH 7 display the greatest β-hairpin variability, consistent with maximum pore flexibility occurring under physiological conditions. The likely reason why a pore has not been detected in published CA$_{Hexamer}$ structures is because they were solved at a basic pH where H12 is deprotonated and a closed pore is favored. To test this hypothesis and demonstrate that the pore can open in the context of an assembled hexamer, we sought to crystallise CA$_{Hexamer}$ under acidic conditions. We obtained a previously unreported crystal form at pH 5.5, the structure of which contains a β-hairpin in the open conformation and an exposed pore (Fig. 1b, far right).

Using all available CA structures to define a range of movement for the β-hairpin, we observed that the pivoting about P1 results in an iris-like motion, which creates an aperture on the outer surface of the capsid (Fig. 2a). In the open state, a chamber 25 Å deep and 3240 Å3 in volume is revealed, which culminates in a ring of six arginine side-chains from residue 18 (Fig. 2b, Supplementary Video 2). This cluster of basic residues in close proximity results in highly electropositive foci at the centre of each hexamer. The R18 residues adopt multiple conformations (Extended Data Fig. 1a) to give a maximum pore diameter of 8 Å, sufficient to allow transit of a dNTP molecule. We therefore reasoned that this feature might provide an efficient means to recruit dNTP's into the capsid interior whilst excluding larger molecules. We therefore tested whether CA$_{Hexamer}$ can interact with dNTP's by fluorescence anisotropy and found that all four nucleotides bind with remarkably high affinity of between 6-40 nM (Fig. 2c). All biophysical measurements were undertaken in an 'intracellular buffer' (see Methods) that is designed to match salt concentrations in the cell. We also

observed that physiological concentrations of inorganic phosphate had little effect on dNTP binding and that the pore could not distinguish between dNTP's and rNTP's (Extended Data Fig. 2) consistent with the observation that rNMP's are often incorporated into newly-synthesised viral DNA13. Analyzing the kinetics of interaction by stopped-flow revealed that binding is driven by an extremely rapid on-rate of $> 2\text{x}10^8$ M^{-1} s^{-1}, although this is likely an underestimate as the reaction becomes immeasurably fast at increasing reactant concentrations (Fig. 2d&e). Separate dissociation experiments in which fluorescent dCTP was displaced with excess unlabeled dCTP determined that the off-rate is also fast at >12 s^{-1} (Fig. 2f), equivalent to a half life of 58 ms. Calculation of on-rates for all four nucleotides based on their steady-state affinities and off-rates confirms that HIV-1 hexamers achieve association rates between 10^8-10^9 M^{-1} s^{-1}. These are unusually rapid association kinetics, typically found in enzymes that have achieved so-called kinetic perfection. Such ultra-rapid enzymes are rare because of the strong fitness advantage needed for their selection over merely very fast equivalents14. The rapid on-rate of dNTP recruitment that HIV achieves may be the result of an electrostatically assisted association binding mechanism, as has been described for barnase/barstar15. Importantly, the combination of fast on and off rates suggests that while the HIV-1 capsid may recruit dNTP's extremely efficiently, these nucleotides quickly dissociate to become available as substrates for reverse transcription.

To test our hypothesis that it is the ring of arginine residues that is responsible for nucleotide recruitment, we solved the structure of HIV-1 CA$_{\text{Hexamer}}$ in complex with dATP and found that it binds as predicted in the center of the arginine ring via its phosphate groups (Fig. 2g). While there is electron density for the phosphates, the position of the base can only be modeled, likely because hexamer rotational symmetry allows the dATP base to occupy six equivalent positions, averaging its density over a large volume (Extended Data Fig. 1). Comparison with a structure solved under identical conditions, but in the absence of dATP, confirms that the observed density corresponds to the nucleotide. To further investigate the importance of R18 in the recruitment of dNTP's, we produced R18G and R18A CA$_{\text{Hexamer}}$ mutants. Neither R18G nor R18A affected the overall structure of the protein and neither displayed measurable nucleotide binding (Fig. 3a&b). To determine whether formation of the arginines into a ring is required, we performed binding experiments on wild-type protein in the presence of DTT, which reduces the disulphide bonds that stabilise the hexameric construct, resulting in monomeric CA. No binding was observed to monomeric CA demonstrating that once the pore is disassembled, the capsid can no longer recruit dNTP's (Fig. 3b).

The concentration of positive charge provided by the R18 ring is an unusual feature and might be expected to exert a destabilizing influence on the capsid lattice. Conversely, it has been calculated that arginine pairs can stabilize protein interfaces16, while arginine clusters have been postulated to have a stabilizing effect17. We performed differential scanning fluorimetry (DSF) to compare the relative stability of CA$_{\text{Hexamer}}$ with and without the electropositive pore. We observed a remarkable stability of the R18G hexamer relative to wild-type complex, corresponding to a surprisingly large increase in T$_{\text{m}}$ of 4 °C (Fig. 3c, Extended Data Fig. 3). A similar increase in stability was observed in wild-type hexamer in the presence of dNTP's, while no stabilization was observed when dNTP's were added to R18G hexamer (Fig. 3d). Taken together, these results suggest that the pore is indeed a

destabilising feature that is tolerated by the capsid lattice in order to facilitate nucleotide binding. An alignment of capsid sequences predicts an electropositive pore to be conserved across retrovirus genera, with the exception of the gammaretroviruses (Extended Data Fig. 4). While there appears to be no R18-equivalent in gammaretroviruses, analysis of the published MLV capsid structure reveals a large channel running down the six-fold axis with an inward facing Arg residue at position 3 (Mortuza *et al.* 2008). This residue may have a role in attracting dNTP's, but it is unlikely that the MLV capsid has the same size-selectivity as the HIV capsid as the pore is much wider.

The observation that HIV-1 has evolved the fastest possible rate constant for nucleotide recruitment suggests that dNTP import may be a limiting factor in reverse transcription and infectivity. To determine how the efficiency of nucleotide recruitment impacts on these measures of viral fitness, we constructed a matched set of chimeric WT:R18G $CA_{Hexamer}$ and viruses (see Extended Data Fig. 5 for chimera controls). R18G was chosen as its capsid morphology has previously been demonstrated to be indistinguishable from WT[19]. Furthermore, R18G was able to saturate the activity of capsid-binding restriction factor TRIM5α, confirming that assembled capsids enter the cytoplasm[20] (Extended Data Fig. 6a). We tested our chimeric hexamers for dNTP binding and found that an incorporation ratio of 5:1 (5 arginines to 1 glycine) had a minimal impact on affinity (Fig. 3e). However, as the proportion of glycine residues was increased, there was a dose-dependent decrease in dNTP binding. Testing HIV-1 GFP VSV-G pseudotyped chimeric viruses for infectivity revealed a similar pattern of R18 dependence, in which there was little change in infectivity at a ratio of 5:1 but a dominant negative effect at higher G18 ratios (Fig. 3f). Assuming a binomial distribution of arginines and glycines in viral hexamers, the data fit a model in which removal of two or more arginines from the pore is detrimental to the virus (Extended Data Fig. 6b,c), which is consistent with the observation that removal of one arginine has little impact on dNTP affinity. Importantly, there is close correlation between chimera infectivity and nucleotide affinity, consistent with the recruitment of dNTP's impacting directly on viral infection (Fig. 3g). Such a mechanism would be expected to influence infection at the level of reverse transcription and indeed a similarly close correlation is observed between chimera affinity and the production of early reverse transcripts (Fig 3h).

We propose that reverse transcription takes place within the protected environment of the capsid by recruiting nucleotides through a strongly electropositive pore at the center of each capsid hexamer. In order to explore this further we performed endogenous reverse transcription (ERT) assays in which HIV-1 capsid cores were purified from virions[21] and their reverse transcriptase activity quantified *in vitro* (Extended Data Fig. 7). Efficient strong-stop reverse transcription (the first DNA synthesis step) was observed upon incubation of cores with dNTP's. Moreover, addition of DNase I, RNase A or the promiscuous nuclease Benzonase failed to prevent encapsidated reverse transcription (Fig. 4a, Extended Data Fig. 7e). This demonstrates that dNTP's can access the interior of the capsid but larger nucleases cannot, supporting the notion of a size selective pore. Processivity beyond strong-stop was observed but at lower efficiency, in agreement with published data[22].

If the R18 pore is responsible for dNTP import, it is conceivable that capsid mutations that affect the movement of the β-hairpin may also affect the efficiency of reverse transcription. Of the residues primarily responsible for the hairpin movement (Fig 1a), P1 and D51 are invariant, with mutations at these positions resulting in non-infectious particles due to defective capsid assembly[12]. His12 is also highly conserved, however, in ~2% of sequences it has been replaced by a tyrosine. As tyrosine is not titratable over physiological pH's, we hypothesised that the H12Y mutation would result in the β-hairpin favouring one conformation. Solving the crystal structure of this mutant revealed that under the high-pH condition, Y12 displaces the bound water molecule and makes a hydrogen-bond contact with Asp51 (Fig. 4b). Despite contacting D51 directly, the larger sidechain of Y12 relative to H12 causes the β-hairpin to favour the closed conformation (Fig. 4c). Importantly H12Y does not completely shut the pore because residues 4-9 do not occupy a single defined state (Extended Data Fig. 8). The β-hairpin therefore retains a degree of flexibility despite rigidification about the P1-D51 'hinge'. Nevertheless we predicted that favouring the closed conformation should result in H12Y having reduced RT kinetics while retaining some infectivity and this is what we observe (Fig. 4d).

To provide further evidence that nucleotides are being recruited through the R18 pore to allow ERT, we sought a small molecule inhibitor that would block the pore. Small polyanionic compounds have been used previously to block analogous arginine-rich pores[23]. We found that the hexacarboxybenzene series (which are polyanionic at physiological pH) bound to $CA_{Hexamer}$ and competed for nucleotide binding as measured by fluorescence anisotropy and DSF, respectively (Fig. 4e&f, Extended Data Fig. 3). Activity broadly increased with the number of negative charges present within the compound, with hexa- or pentacarboxybenzene being the most effective. DSF indicated that the compounds did not bind in the absence of R18 or when hexamers were reduced by DTT, and the crystal structure of the hexacarboxybenzene-bound $CA_{Hexamer}$ confirmed that the compound was co-ordinated by R18 within the central pore (Fig. 4f&g). At sufficiently high concentration, tetra-, penta- and hexacarboxybenzene fully inhibit reverse transcriptase, presumably by competing with dNTP's (Extended Data Fig. 7f). However, in ERT assays, when reverse transcriptase is enclosed within an intact viral capsid, tetracarboxybenzene has no effect on reverse transcription, with only a small effect observed for pentacarboxybenzene (Fig. 4h). In contrast, hexacarboxybenzene inhibited ERT almost completely. The failure of tetracarboxybenzene to inhibit ERT demonstrates that a compound sufficiently small to pass through the channel is still efficiently excluded from the capsid interior if it cannot bind the pore. This result emphasises the chemical selectivity of the pore and its role in dNTP import during reverse transcription.

As a semi-permeable reaction chamber, the HIV-1 capsid is reminiscent of bacterial microcompartments – primitive 'organelles' that utilize a protein coat to isolate toxic reaction intermediates from the cytoplasm[24]. Microcompartments import substrates through a size-selective pore to be consumed by enzymes located inside a chamber[25]. Similarly, dNTP's translocated inside the HIV capsid will be hydrolysed by encapsidated reverse transcriptase. Coupling import with hydrolysis may create a local chemical gradient, promoting interior movement despite the release of captured dNTP's on either side of the pore. Appositely, a subset of microcompartments, carboxysomes, contain positively charged

amino acids that are thought to selectively transport bicarbonate and ribulose-1,5-bisphosphate over uncharged CO_2 and $O_2$26. Some microcompartment structures have gated channels located at the six-fold axes in their protein lattice, to control substrate entry and product release. The fact that a similar 'gate' potentially exists in the HIV-1 capsid, provided by the 'molecular iris' of the β-hairpin, suggests that the virus could use this as a mechanism to regulate reverse transcription. In addition, the regulation of capsid stability through dNTP recruitment, and possibly DNA synthesis, provides a model whereby HIV-1 may co-regulate DNA synthesis and uncoating to facilitate cytoplasmic DNA synthesis that remains invisible to cytoplasmic DNA sensing. Finally, the high degree of conservation of R18 coupled with the fact that the pore can be obstructed chemically identifies the pore as a novel target for drug development.

Methods

Protein production and purification

The CA N-terminal domain and the disulfide-stabilised $CA_{Hexamer}$ were expressed and purified as previously described8,27. The R18G mutation was introduced by QuikChange site-directed mutagenesis. Chimeric $CA_{Hexamers}$ were produced by mixing the desired ratio of pre-assembled WT and R18G $CA_{Hexamer}$ (16 mg/ml) followed by a four-step dialysis: i) Disassembly in TRIS (pH 8.0, 50mM), NaCl (40 mM), β-mercaptoethanol (20 mM); ii) Reassembly in TRIS (pH 8.0, 50 mM), NaCl (1 M), β-mercaptoethanol (20 mM); iii) Oxidation in TRIS (pH 8.0, 50 mM), NaCl (1 M); Redispersion in TRIS (pH 8.0, 20 mM), NaCl (40 mM). In the context of the chimera experiments, WT and R18G were also subjected to this process so that samples were matched with the other ratios. Reassembled hexamers were observed by non-reducing SDS-PAGE. Chimeric hexamers were compared with mixes of homohexamers by fluorescence anisotropy (see below and Extended Data Fig. 5) in order to demonstrate that chimeras had indeed formed.

Crystallisation, structure solution and analysis

All crystals were grown at 17 °C by sitting-drop vapour diffusion in which 100 nL protein was mixed with 100 nL precipitant and suspended above 80 uL precipitant. The CA N-terminal domain (15 mg/ml) 'open' conformation was crystallised from PEG3350 (20%), Ammonium chloride (0.2 M, pH 6.3). Crystals were cryoprotected in precipitant supplemented with 25% glycerol. The $CA_{Hexamer}$ (15 mg/ml) 'open conformation' was crystallised from PEG4000 (12%), NaCl (0.1 M), $MgCl_2$ (0.1 M), sodium citrate (0.1 M, pH 5.5). Crystals were cryoprotected in precipitant supplemented with 20% MPD. The remaining $CA_{Hexamer}$ structures (apo, dATP-bound, R18G and hexacarboxybenzene-bound) were all obtained from 10-12 mg/ml protein mixed with PEG550MME (13-14%), KSCN (0.15 M), TRIS (0.1 M, pH 8.5) and cryoprotected with precipitant supplemented with 20% MPD. For the dATP-bound structure, the protein was supplemented with 10 mM dATP immediately prior to crystallisation; while for the hexacarboxybenzene structure, the protein was likewise supplemented with 1 mM hexacarboxybenzene (TRIS-buffered to pH 8.0). All crystals were flash-cooled in liquid nitrogen and data collected either in-house using Cu $K\alpha$ X rays produced by a Rigaku FR-E rotating anode generator with diffraction recorded on a mar345 image plate detector (marXperts), or at beamline I02 at Diamond Light Source. The

datasets were processed using the CCP4 program suite28. Data were indexed and integrated with IMOSFLM29 and scaled and merged with either POINTLESS and SCALA30 or AIMLESS31. Structures were solved by molecular replacement using PHASER32 and refined using REFMAC533. Between rounds of refinement, the model was manually checked and corrected against the corresponding electron-density maps in COOT34. Solvent molecules and bound ligands were added as the refinement progressed either manually or automatically within COOT and were routinely checked for correct stereo-chemistry, for sufficient supporting density above a 2Fo-Fc threshold of 1.0σ and for a reasonable thermal factor. The quality of the model was regularly checked for steric clashes, incorrect stereochemistry and rotamer outliers using MOLPROBITY35. Final figures were rendered in The PyMOL Molecular Graphics System, Version 1.5.0.4 Schrödinger, LLC. Surface electrostatics were calculated using the APBS PyMOL plugin36 and cavity volume measurements with 3V37. Data collection and refinement statistics are presented in Extended Data Table 2. The 'fullerene cone' model of an HIV-1 virion is based on 3J3Q38 but using the inter-hexamer packing from 4XFY39 and an open β-hairpin conformation.

Fluorescence Anisotropy

Fluorescence anisotropy measurements were performed at 22 °C on a Cary Eclipse Fluorescence Spectrophotometer (Agilent). Fluorescein-labelled dNTP's were obtained from Perkin Elmer and used for saturation binding experiments at a concentration of 2 nM prepared in 'Intracellular Buffer': potassium gluconate (110 mM), KCl (25 mM), NaCl (5 mM), $MgCl_2$ (2 mM), HEPES (10 mM), final pH 7.2. $CA_{Hexamer}$ disassembly was achieved by the addition of DTT (4 mM), and was performed routinely at the conclusion of each saturation binding experiment to confirm the absence of non-specific binding. It was found that the triphosphate was not stable over the timescale of the competition binding experiments; so fluorescein-labelled dNTP's were substituted for a non-hydrolysable BODIPY-labelled GTP-γ-S (ThermoFisher Scientific). Saturation binding experiments determined that this non-hydrolysable analogue bound with unchanged affinity to the $CA_{Hexamer}$ (K_d = 14 nM). 200 mM stock solutions of hexacarboxybenzene (Sigma), pentacarboxybenzene (MP Biomedicals), 1,2,4,5-tetracarboxybezene (Sigma), and 1,3,5-tricarboxybenzene (Fluka) were prepared in 50mM TRIS and adjusted to pH 8.0. For competition binding experiments, the competitor was titrated into a mix of $CA_{Hexamer}$ (28 nM) and BODIPY-GTP-γ-S (2 nM). All fluorescence anisotropy measurements are representative of at least two experiments. Each point is measured in quadruplicate and plotted as mean ± standard deviation. In many cases error bars lie within the datapoint. Saturation binding and competition binding curves were fit using GraphPad Prism (GraphPad Software, Inc.).

Rapid reaction kinetics

Experiments were carried out using a dual-channel fluorescence TgK single-mix SF-61SX2 stopped-flow spectrometer. All samples were prepared in Intracellular Buffer. Mixing was performed 1:1, using an excitation wavelength of 488 nm and a 520 nm cutoff filter. Association experiments were carried out at 0.25 μM dCTP and a range of μM $CA_{Hexamer}$ concentrations. Dissociation experiments were carried out using 20 μM unlabeled dCTP and a pre-formed fluorescein-labeled 1 μM dCTP: $CA_{Hexamer}$ complex. Relaxation rates were

determined using a single exponential model: $F = \Delta F \exp(-k_{obs}t) + F_e$, where F is the observed fluorescence, ΔF is the fluorescence amplitude, k_{obs} is the observed pseudo first-order rate constant, and F_e is the end-point fluorescence. The bimolecular association rate constant (k_{on}) was determined by fitting the linear relationship between k_{obs} and the increasing pseudo-first order concentrations of $CA_{Hexamer}$ to: $k_{obs} = k_{on}[CA_{Hexamer}] + k_{reverse}$. For stopped flow experiments, every 0.5 s measurement included >2000 datapoints, each of which was oversampled 99 times. At least three independent mixing experiments were averaged for each ligand concentration.

Differential Scanning Fluorimetry

DSF measurements were performed using a Prometheus NT.48 (NanoTemper Technologies) over a temperature range of 20-95 °C using a ramp rate of 2.5 °C/min. $CA_{Hexamer}$ samples were prepared at a final concentration of 1mg/ml in Intracellular Buffer (+/- DTT (4 mM)). dNTP's or competitors were added at 200 μM. DSF scans are single reads. Consistency between like points yields an uncertainty in T_m of no greater than 0.2 °C.

Cells and Viruses

All cell lines were obtained from ATCC and tested negative for mycoplasma contamination. Replication deficient VSV-G pseudotyped HIV GFP vectors were produced in HEK293T cells as described previously[3]. Site-directed mutagenesis of CA was performed using the QuikChange method (Stratagene) against the Gag-Pol expression plasmid, pCRV-1. Chimeric viruses were produced by mixing the appropriate ratio of WT or mutant pCRV-1 prior to transfection. Reverse transcriptase activity was quantified using a colorimetric ELISA assay (Roche) and was found not to vary significantly between viruses. Production of mature particles was confirmed by western blot for p24 from pelleted virus, with no observable difference between chimeras. Primary antibody used for western blotting was a polyclonal goat anti-p24 (Bio-Rad, product 4999-9007).

Infection Experiments

Infections of HeLa cells were performed in the presence of 5 μg/ml polybrene. GFP expressing cells were enumerated on a BD LSRII Flow Cytometer (BD Biosciences) 2 days post-transfection after fixation of cells in 4% paraformaldehyde. Chimera infectivity was determined by a 6-point titration of each chimera onto HeLa cells. Values are the mean ± standard deviation calculated from all points for which the proportion of infected cells after 48 h was between 1% and 50%.

TRIM5α Abrogation Assay

'Abrogating virus' (VSV-G pseudotyped HIV Puromycin vectors) was produced as described above, with the exception that the *gfp* gene was replaced with the *pac* gene to ensure the virus did not confer fluorescence upon infection. Virus was concentrated by ultracentrifugation with an SW28 rotor at 25,000 rpm for 2 h. The abrogating virus capsids were WT, R18G or W184A/M185A (a mutant with a known assembly defect that cannot compete for TRIM5α). VSV-G pseudotyped HIV GFP vectors were titrated on FRhK-4 cells in the presence of 5 μg/ml polybrene to determine the volume of virus required to achieve

1% infection. In a separate experiment, cells were then coinfected with that amount HIV-GFP vector and a titration of VSV-G pseudotyped HIV Puromycin vectors (the abrogating virus). GFP expressing cells were measured in duplicate and enumerated as above. Results are representative of three experiments and are presented as mean ± standard deviation. For many points the error bars lie within the datapoint.

Quantitative PCR

For analysis of reverse transcription products, viral supernatant was treated with 250 U/ml DNase (Millipore) for 1 h prior to infection. Cells were harvested 6h post infection. DNA was extracted using DNeasy Blood and Tissue Kit (Qiagen). GFP copies were quantified using primers GFPF (CAACAGCCACAACGTCTATATCAT), GFPR (ATGTTGTGGCGGATCTTGAAG) and probe GFPP (FAM-CCGACAAGCAGAAGAACGGCATCAA-TAMRA) against a standard curve of CSGW on an ABI StepOnePlus Real Time PCR System (Life Technologies). Chimera reverse transcription measurements are representative of 3 experiments with each point measured in triplicate. Results are presented as mean ± standard deviation. For H12Y, a timecourse was also performed, in which each time point was measured in triplicate and presented as above.

Preparation of HIV-1 cores

HIV-1 capsid cores were prepared using a protocol based on[21] with modifications. 90ml HEK293T supernatant containing VSV-G pseudotyped HIV-1 GFP was pelleted over 20% sucrose dissolved in core prep buffer (CPB; 20 mM Tris pH 7.4, 20 mM NaCl, 1 mM MgCl$_2$) in an SW28 rotor (Beckman) at 25,000 rpm at 4 °C. Pellets were gently resuspended at 4 °C in CPB for 1 h with occasional agitation. Resuspended pellets were treated with DNase I from bovine pancreas (Sigma Aldrich) for 1 h at 200 µg/ml at room temperature to remove contaminating extra-viral DNA. Virus was subjected to spin-through detergent stripping of the viral membrane as follows. A gradient at 80-30% sucrose was prepared in SW40Ti ultracentrifuge tubes and overlaid with 250 µl 1% Triton X-100 in 15% sucrose, followed by 250 µl 7.5% sucrose. All solutions were prepared in CPB. 750 µl DNase-treated, concentrated virus was layered on top of the gradient and subjected to 32,500 rpm at 4 °C for 16 h. The preparation was fractionated and the location of cores was determined by ELISA for p24 (Perkin Elmer). Core-containing fractions were pooled and snap frozen before storage at -80 °C.

Endogenous reverse transcription assays

Viral cores were diluted to 400 µg/ml p24 with 60% sucrose in CPB and pre-treated with nucleases for 1h before addition of dNTPs. Final concentrations of dNTP's were 100 µM each, DNase I and RNase A were at 100 µg/ml and Benzonase was at 250 U/ml. 20 µl reactions were incubated at room temperature for 16 h unless indicated otherwise and were stopped by shifting to -80 °C. DNA was prepared using DNeasy Blood and Tissue kit (Qiagen) after addition of 200 µl PBS with of 50 µg/ml salmon sperm carrier DNA to each sample. Reverse transcript products were detected using TaqMan Fast Universal PCR Mix (ABI) and RU5 primers to detect strong stop DNA[40] (RU5 fwd TCTGGCTAACTAGGGAACCCA, RU5 rev CTGACTAAAAGGGTCTGAGG and RU5 probe FAM-TTAAGCCTCAATAAAGCTTGCCTTGAGTGC-TAMRA), GFP primers to

detect first strand transfer products (described above) and primers for second strand transfer products40 (2ST fwd TTTTAGTCAGTGTGGAAAATCTGTAGC, 2ST rev TACTCACCAGTCGCCGCC and 2ST probe FAM-TCGACGCAGGACTCGGCTTGCT-TAMRA). Where used, carboxybenzene compounds were dissolved in CPB, pH adjusted with NaOH and added to reactions at a final concentration of 20mM. In order for dNTP concentration to be limiting, these reactions were performed in the presence of 1 μM each dNTP and reactions were stopped 5 h after their addition. ERT experiments were performed in experimental triplicate and are representative of several experimental replicates. Data are represented as mean ± sem
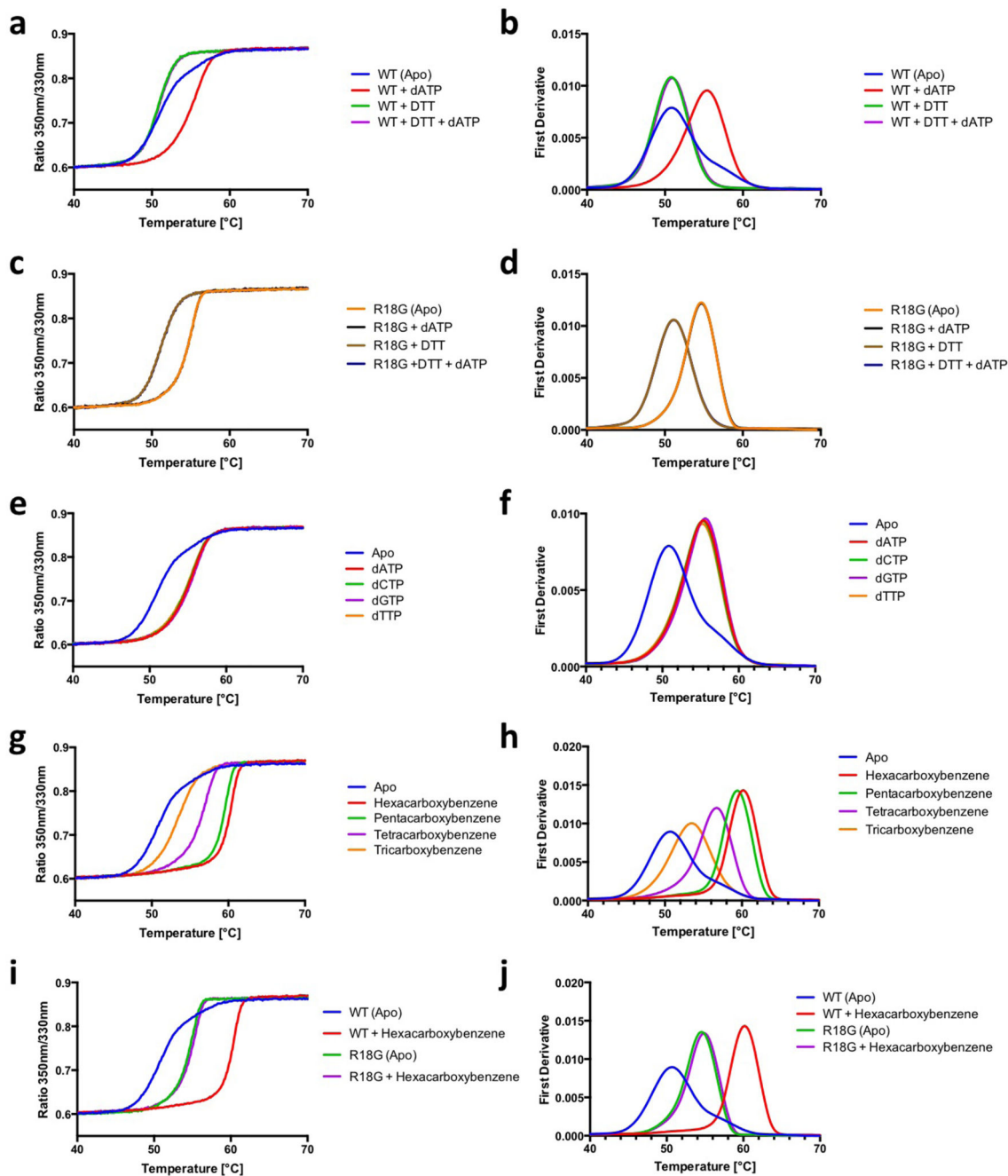
Extended Data
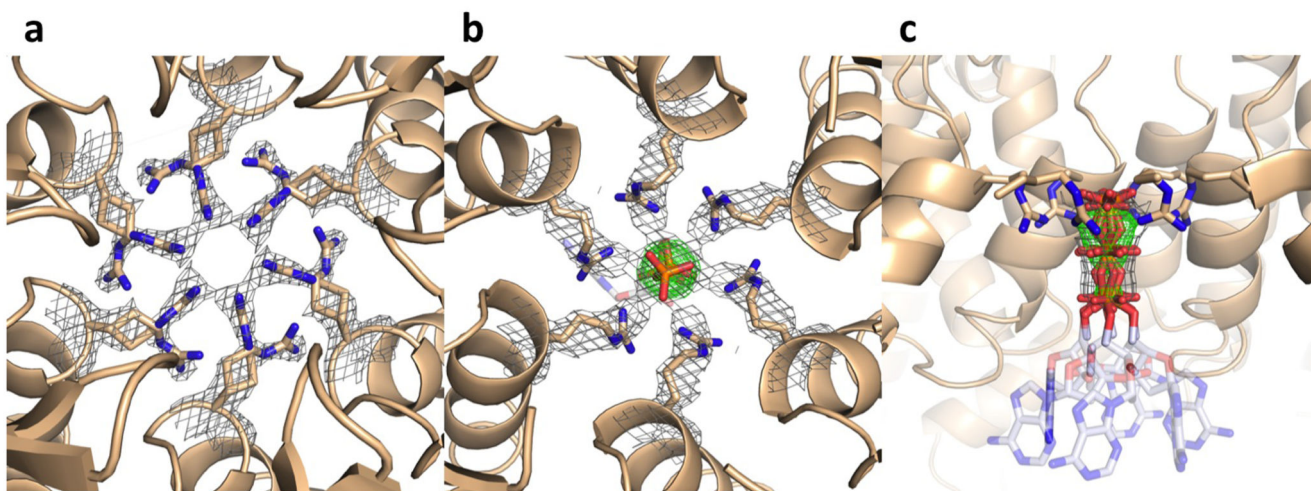
Extended Data Figure 1. dATP binds to the R18 pore at the centre of the capsid hexamer.
2Fo-Fc density (grey mesh) contoured at 1.0σ about R18 for the unbound (**a**) and dATP-bound (**b**) CA$_{Hexamer}$ structures. Fo-Fc omit density (green mesh) contoured at 3.0σ is shown for the dATP-bound structure. **c**, dATP lies on the crystallographic 6-fold axis and significant rotationally-averaged density is observed only for the triphosphate group.
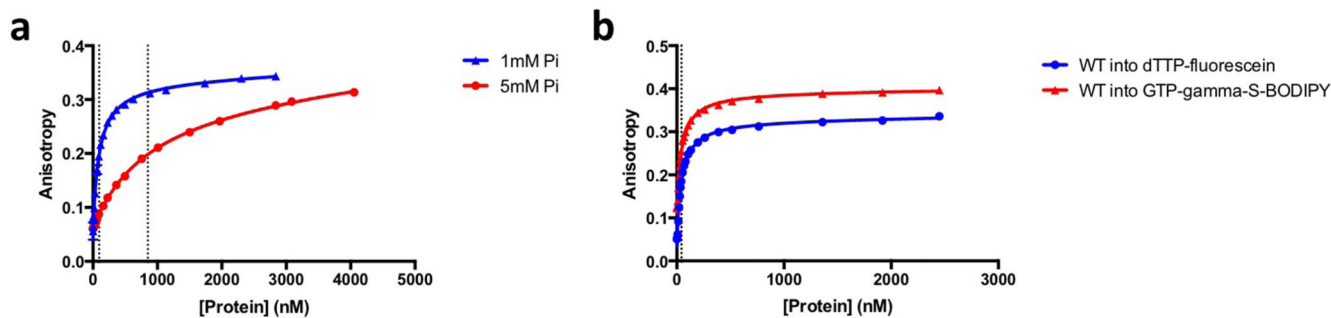
Extended Data Figure 2. Controls for dNTP-binding experiment.
**a**, Titration of CA$_{Hexamer}$ into 2 nM fluorescein-labelled dTTP in the presence of 1 mM (physiological) or 5 mM inorganic phosphate. Under the 1 mM conditions, there is no significant effect on hexamer binding to dTTP. At 5 mM apparent affinity is decreased to

851 nM, demonstrating that inorganic phosphate can compete for the pore. However, given that the intracellular [dNTP] is approximately 100 μM, under intracellular conditions dNTP binding would dominate. **b**, Titration of $CA_{Hexamer}$ into BODIPY-labelled rGTP-γ-S and fluorescein-labelled dTTP. Each binds with the same affinity suggesting that the R18 pore is unable to discriminate between ribose and deoxyribose nucleoside triphosphates. The difference in the magnitude of the fluorescence anisotropy signals is due to differences in fluorophore excited state lifetimes. K_D values are indicated by a dotted line.

Extended Data Figure 3. DSF melt curves.

The left-hand panels report the ratio of tryptophan fluorescence emission at 350nm and 330nm as a function of temperature. The right-hand panels report the first derivative of the same data, the peak of which is used to determine the T_m value. **a, b**, Effect of dATP and DTT on WT $CA_{Hexamer}$. **c, d**, Effect of dATP and DTT on R18G $CA_{Hexamer}$. **e, f**, Effect of each dNTP on WT $CA_{Hexamer}$. **g, h**, Comparison of the effects of carboxybenzene compounds on WT $CA_{Hexamer}$. **i, j**, Comparison of the effects of hexacarboxybenzene on WT and R18G $CA_{Hexamer}$.
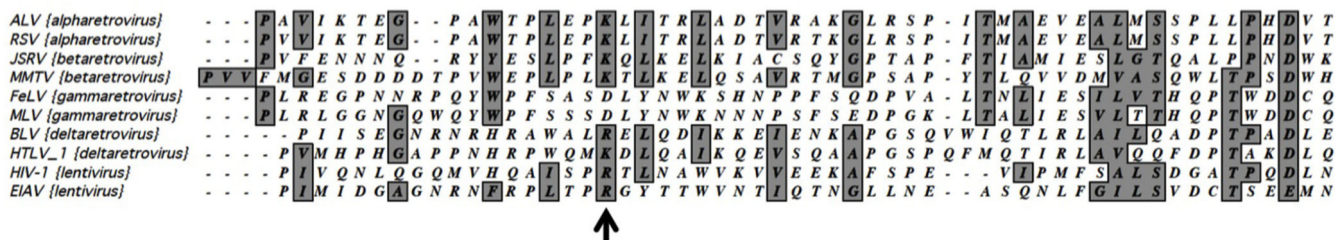

Extended Data Figure 4. Alignment of selected retrovirus capsid sequences bordering the electropositive pore.

The position equivalent to R18 in HIV-1 is marked with an arrow.
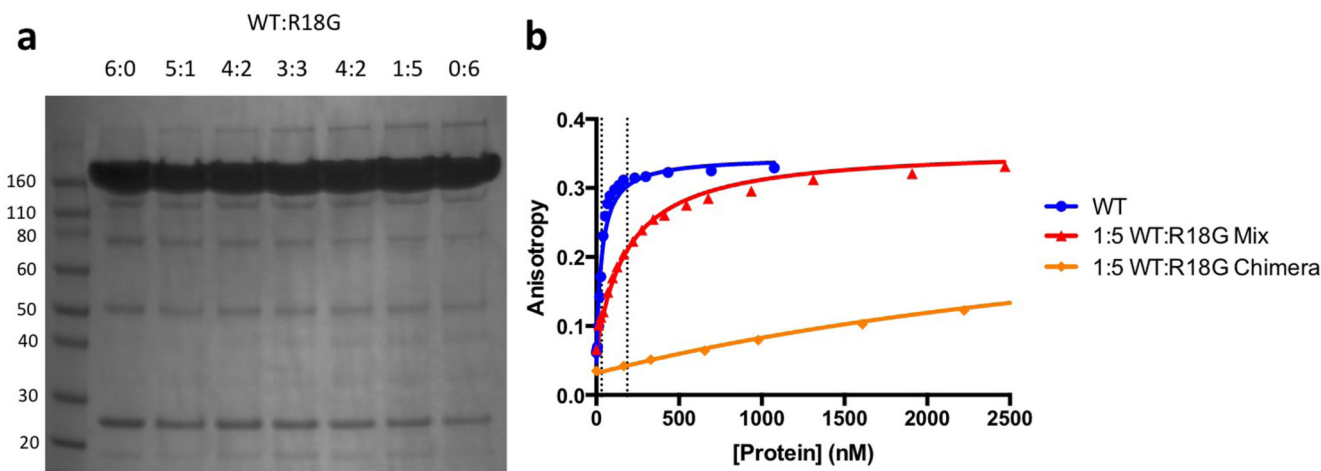
**Extended Data Figure 5. Confirmation of $CA_{Hexamer}$ Chimera Assemblies.**

a, Non-reducing SDS-PAGE of $CA_{Hexamer}$ WT:R18G chimera samples demonstrates that the recombinant proteins had reassembled into hexamers. Molecular weight standards (kDa) are presented in the first lane. For gel source data, see Supplementary Fig. 1. **b**, Comparison of 1:5 homohexamer mix and the equivalent chimera. The 1:5 WT:R18G mix experiences a six-fold loss of apparent K_d, as expected for a 6-fold dilution of WT with a non-binding mutant. In contrast, the 1:5 chimera chimera has a 58-fold decrease in K_d, demonstrating that chimeric hexamers had indeed formed.
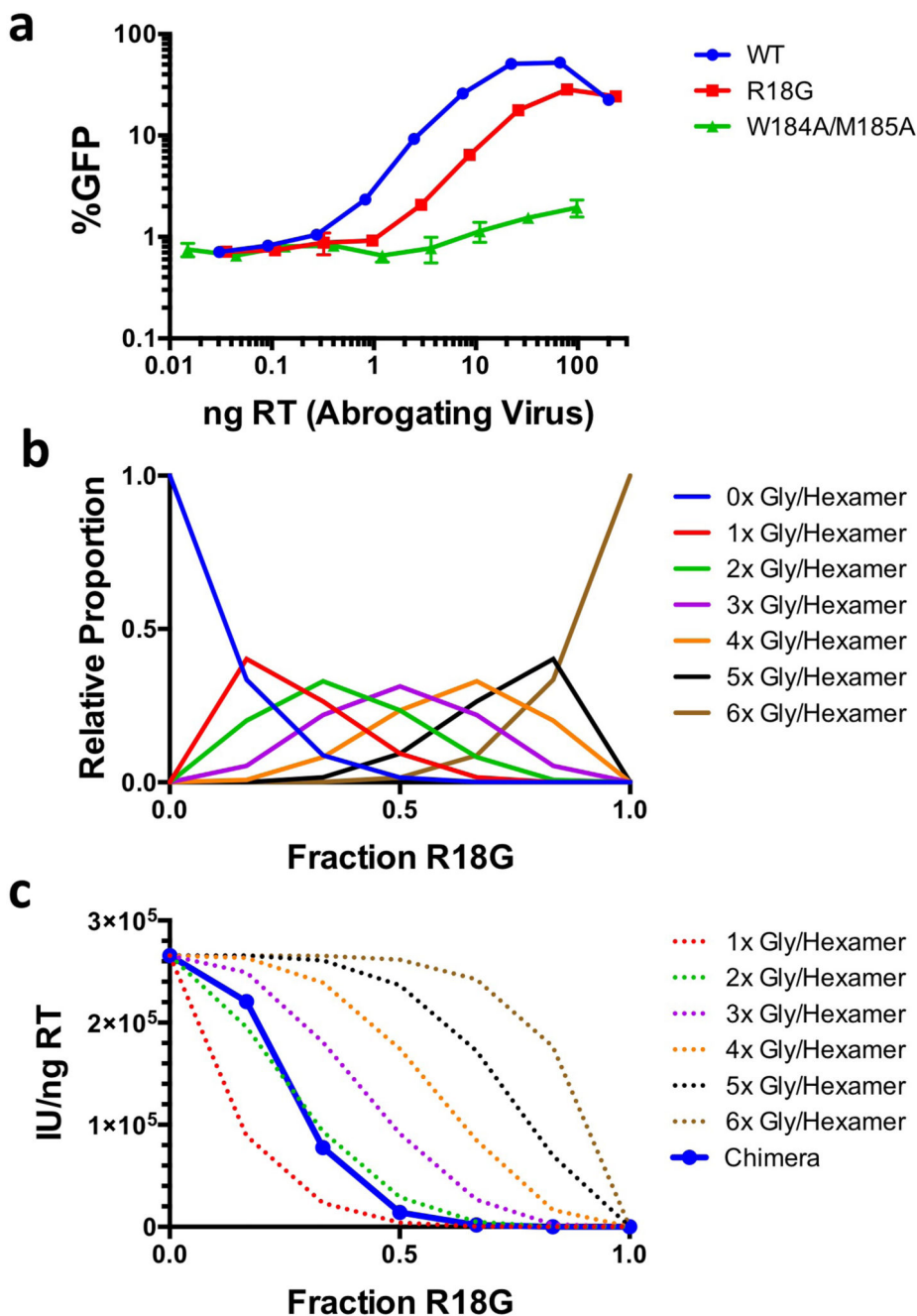
Extended Data Figure 6. Effects of HIV-1 CA R18G on viral infectivity.
a, R18G is capable of abrogating TRIM5α-mediated restriction. Rhesus TRIM5α provides a potent block to infection of HIV in FRhK-4 cells. Titration of a non-GFP-expressing virus can compete for TRIM5α-binding and relieve the restriction of a GFP-expressing virus only if it delivers an assembled capsid into the cytoplasm. R18G abrogates restriction but W184A/M185A, which is incapable of forming assembled capsids due to loss of the CTD-CTD dimerization interface, does not. **b**, Binomial distribution model for the relative proportion of capsid hexamers carrying a discrete number of glycines at position 18 at

defined bulk ratios of WT:R18G. **c**, Six models (dotted lines) predicting the effect of replacing arginine 18 with glycines. Each model assumes a different number of glycines is required to render the pore defective. The data from WT:R18G chimeric virus measurements (solid line) is consistent with a model in which four or more arginines (i.e. 2 or fewer glycines, green) are required to maintain a functional pore.
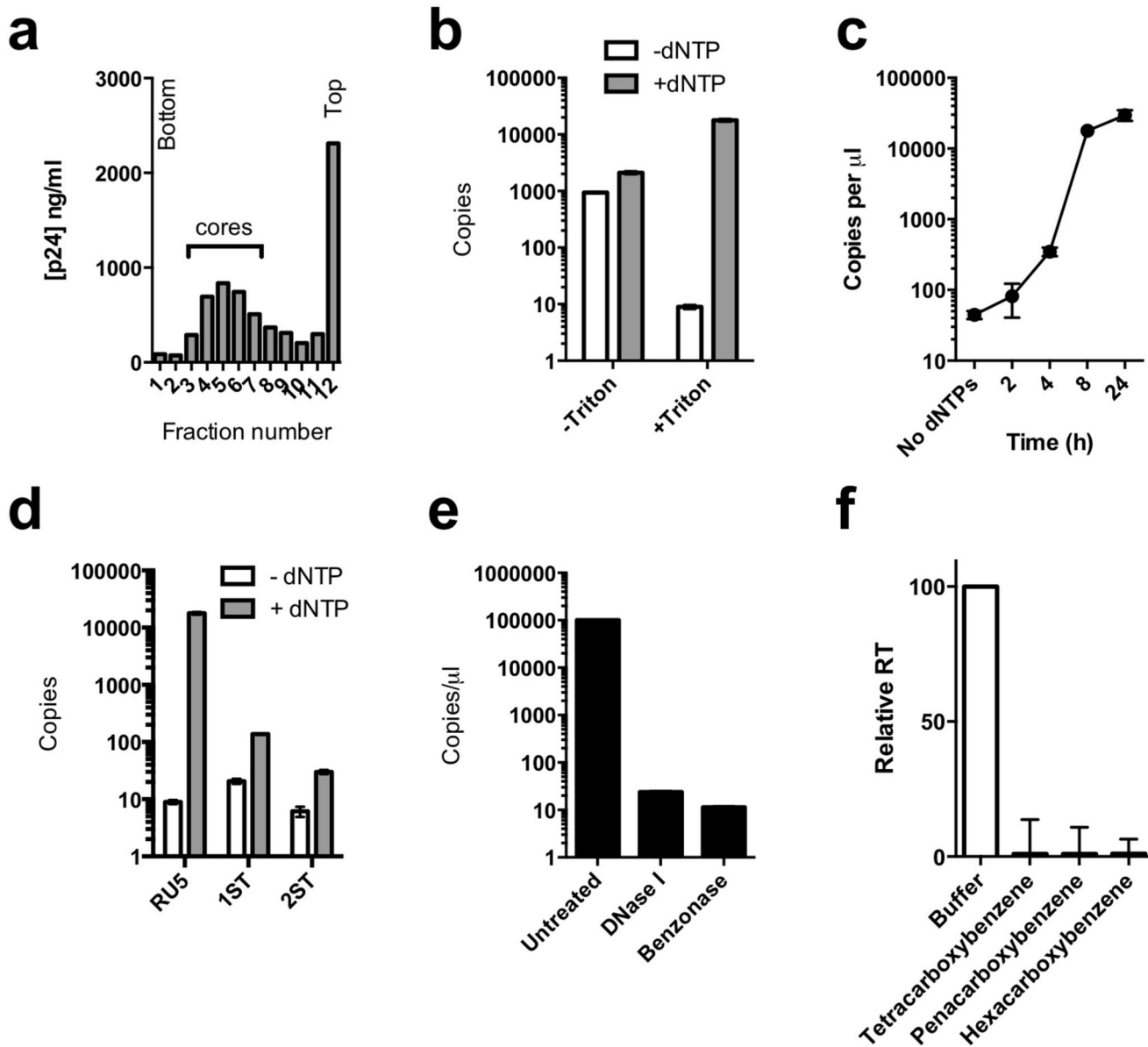
Extended Data Figure 7. ERT assay.
a, HIV-1 cores were prepared by ultracentrifugation through a Triton X-100 layer over a sucrose gradient. Resulting fractions were subjected to ELISA for p24 and fractions 3 – 7 were pooled for further experiments. **b**, Endogenous RT activity for strong stop in the presence of DNase I using HIV-1 fractions that were prepared with or without the Triton X-100 spin-through layer. Input levels of p24 were normalized between reactions. **c**, dNTP's

were added to HIV-1 cores prepared by Triton X-100 spin-through in the presence of DNase I. Reactions were stopped at the indicated time point by shifting to -80° C and levels of strong stop were quantified. **d**, Levels of strong-stop (RU5), first-strand transfer (1ST) and second-strand transfer (2ST) DNA after overnight incubation of HIV-1 cores with or without dNTP's in the presence of DNase I. **e**, Levels of naked HIV-1 DNA genomes untreated or incubated overnight with DNase I or Benzonase. **f**, Effect of carboxybenzene compounds on recombinant reverse transcriptase activity.
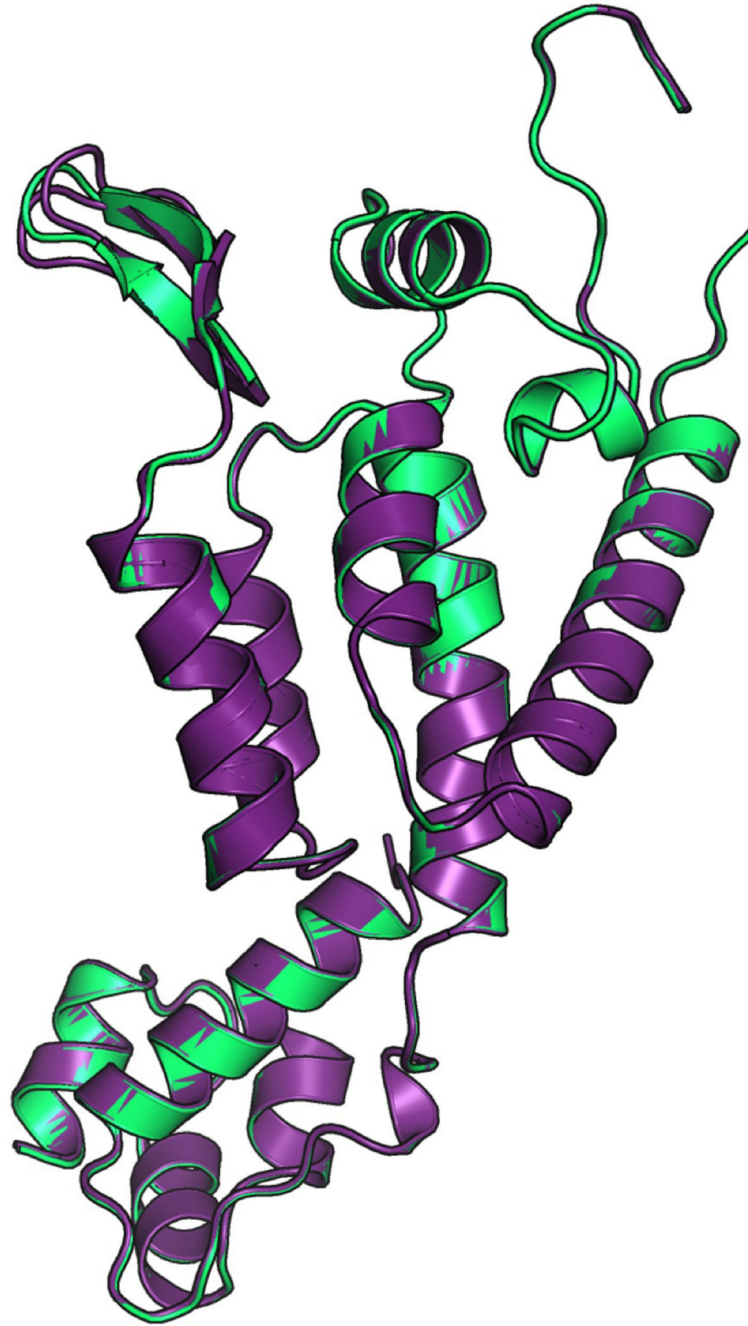
Extended Data Figure 8. Comparison of WT and H12Y crystal structures.

The H12Y monomer (in the context of the hexamer, purple) superposes on the WT (green) with RMSD = 0.2471 Å. Residues 4-9 of the H12Y structure have been modeled in two alternate conformations owing to flexibility towards the tip of the hairpin.

Extended Data Table 1
Details of structures used for β-hairpin analysis

Molecule	Chain	Resolution	Crystallization PH	Q7 Displacemant	H12-D51 distance
5HGL	A	3.1	5.5	3	2.9
5HGL	B	3.1	5.5	2.5	3.1
5HGK	A	1.76	6.3	0	2.7
5HGK	B	1.76	6.3	2.9	2.7
3NTE	A	1.95	6.5	2	2.9
3NTE	B	1.95	6.5	3.8	2.8
2X83	A	1.7	7	7.8	3.7
1AK4	C	2.36	7	10	4.8
2X83	B	1.7	7	9.2	4.5
4B4N	A	1.81	7	13.1	4.9
3H4E	A	2.7	7.5	10.4	4.6
2GON	C	1.9	8	11.9	4.8
3P05	B	2.5	8.5	14.8	4.6
3P05	C	2.5	8.5	10.7	4.6

Extended Data Table 2

Crystallographic data collection and refinement statistics

	CA$_{NTD}$ (OPEN)	CA$_{Hexamer}$ (OPEN)	CA$_{Hexamer}$ + dATP	CA$_{Hexamer}$ (APO, CLOSED)	CA$_{Hexamer}$ (R18G)	CA$_{Hexamer}$ + hexacarboxy-benzene	CA$_{Hexamer}$ (H12Y)
Data collection							
Space group	P2$_1$	C222$_1$	P6	P6	P6	P6	P6
Cell dimensions							
a, b, c (Å)	43.72, 23.85, 129.55	89.69, 159.27, 249.40	90.81, 90.81, 56.68	90.73, 90.73, 56.75	90.81, 90.81, 56.88	90.76, 90.76, 56.76	90.60, 90.60, 56.93
α, β, γ (°)	90, 96.31, 90	90, 90, 90	90, 90, 120	90, 90, 120	90, 90, 120	90, 90, 120	90, 90, 120
Resolution (Å)	39.87-1.76 (1.86-1.76)	19.99-3.10 (3.27-3.10)	45.98-2.03 (2.08-2.03)	26.69-1.90 (1.94-1.90)	46.09-2.00 (2.05-2.00)	45.38-1.95 (2.00-1.95)	56.93-1.70 (1.73-1.70)
R_{merge}	0.065 (0.227)	0.094 (0.552)	0.112 (0.551)	0.121 (0.748)	0.166 (0.831)	0.105 (0.862)	0.095 (0.813)
$I/\sigma I$	13.3 (5.0)	7.1 (1.9)	8.2 (1.9)	8.3 (2.1)	6.5 (1.9)	11.7 (2.1)	9.0 (2.4)
Completeness (%)	91.9 (80.6)	97.4 (92.0)	94.9 (69.1)	99.8 (100.0)	100.0 (100.0)	97.9 (99.5)	95.1 (94.7)
Redundancy	4.6 (4.6)	2.4 (2.4)	2.9 (2.4)	5.1 (4.8)	6.0 (5.9)	6.8 (6.5)	4.8 (4.9)
Refinement							
Resolution (Å)	39.87-1.76 (1.81-1.76)	19.99-3.10 (3.18-3.10)	45.98-2.04 (2.10-2.04)	26.69-1.90 (1.95-1.90)	39.32-2.00 (2.05-2.00)	45.38-1.95 (2.00-1.95)	56.93-1.70 (1.74-1.70)
No. reflections	23837 (1552)	30312 (2044)	15488 (1084)	19999 (1468)	17285 (1246)	18188 (1347)	26370 (1949)
R_{work} / R_{free}	0.190/0.224 (0.233/0.286)	0.250/0.281 (0.368/0.399)	0.236/0.263 (0.316/0.384)	0.200/0.225 (0.266/0.342)	0.205/0.221 (0.216/0.255)	0.194/0.221 (0.266/0.299)	0.197/0.232 (0.265/0.285)
No. atoms							
Protein	2284	9358	1558	1623	1605	1612	1688
Ligand/ion	1	193	30	-	-	24	-
Water	338	-	82	124	105	119	123
B-factors							
Protein	27.928	54.173	26.577	30.265	27.732	30.878	27.523
Ligand/ion	38.516	83.117	109.040	-	-	95.409	-
Water	24.730	-	30.031	35.719	28.567	34.088	33.604
R.m.s deviations							
Bond lengths (Å)	0.007	0.008	0.007	0.007	0.007	0.008	0.006
Bond angles (°)	1.222	1.156	0.991	0.998	1.046	1.281	1.009

Supplementary Material

Refer to Web version on PubMed Central for supplementary material.

Acknowledgements

References

1. Campbell EM, Hope TJ. HIV-1 capsid: the multifaceted key player in HIV-1 infection. Nat Rev Microbiol. 2015; 13:471–483. [PubMed: 26179359]

2. Rasaiyaah J, et al. HIV-1 evades innate immune recognition through specific cofactor recruitment. Nature. 2013; 503:402–405. [PubMed: 24196705]

3. Price AJ, et al. Host cofactors and pharmacologic ligands share an essential interface in HIV-1 capsid that is lost upon disassembly. PLoS pathogens. 2014; 10:e1004459. [PubMed: 25356722]

4. Arhel NJ, et al. HIV-1 DNA Flap formation promotes uncoating of the pre-integration complex at the nuclear pore. Embo J. 2007; 26:3025–3037. [PubMed: 17557080]

5. Gamble TR, et al. Crystal structure of human cyclophilin A bound to the amino-terminal domain of HIV-1 capsid. Cell. 1996; 87:1285–1294. [PubMed: 8980234]

6. Kelly BN, et al. Implications for viral capsid assembly from crystal structures of HIV-1 Gag(1-278) and CA(133-278)(N). Biochemistry-Us. 2006; 45:11257–11266.

7. Ylinen LMJ, et al. Conformational Adaptation of Asian Macaque TRIMCyp Directs Lineage Specific Antiviral Activity. PLoS pathogens. 2010; 6

8. Pornillos O, et al. X-Ray Structures of the Hexameric Building Block of the HIV Capsid. Cell. 2009; 137:1282–1292. DOI: 10.1016/j.cell.2009.04.0634 [PubMed: 19523676]

9. Du SC, et al. Structure of the HIV-1 Full-Length Capsid Protein in a Conformationally Trapped Unassembled State Induced by Small-Molecule Binding. Journal of molecular biology. 2011; 406:371–386. [PubMed: 21146540]

10. Pornillos O, Ganser-Pornillos BK, Yeager M. Atomic-level modelling of the HIV capsid. Nature. 2011; 469

11. Price AJ, et al. CPSF6 defines a conserved capsid interface that modulates HIV-1 replication. PLoS pathogens. 2012; 8:e1002896. [PubMed: 22956906]

12. von Schwedler UK, et al. Proteolytic refolding of the HIV-1 capsid protein amino-terminus facilitates viral core assembly. Embo J. 1998; 17:1555–1568. [PubMed: 9501077]

13. Kennedy EM, Amie SM, Bambara RA, Kim B. Frequent incorporation of ribonucleotides during HIV-1 reverse transcription and their attenuated repair in macrophages. The Journal of biological chemistry. 2012; 287:14280–14288. [PubMed: 22383524]

14. Bar-Even A, Milo R, Noor E, Tawfik DS. The Moderately Efficient Enzyme: Futile Encounters and Enzyme Floppiness. Biochemistry-Us. 2015; 54:4969–4977.

15. Schreiber G, Fersht AR. Rapid, electrostatically assisted association of proteins. Nature structural biology. 1996; 3:427–431. [PubMed: 8612072]

16. Magalhaes A, Maigret B, Hoflack J, Gomes JN, Scheraga HA. Contribution of unusual arginine-arginine short-range interactions to stabilization and recognition in proteins. Journal of protein chemistry. 1994; 13:195–215. [PubMed: 8060493]

17. Neves MA, Yeager M, Abagyan R. Unusual arginine formations in protein function and assembly: rings, strings, and stacks. The journal of physical chemistry B. 2012; 116:7006–7013. [PubMed: 22497303]

18. Mortuza GB, et al. Structure of B-MLV capsid amino-terminal domain reveals key features of viral tropism, gag assembly and core formation. Journal of molecular biology. 2008; 376:1493–1508. [PubMed: 18222469]

19. Rihn SJ, et al. Extreme genetic fragility of the HIV-1 capsid. PLoS pathogens. 2013; 9:e1003461. [PubMed: 23818857]

20. Keckesova Z, Ylinen LM, Towers GJ. The human and African green monkey TRIM5alpha genes encode Ref1 and Lv1 retroviral restriction factor activities. Proceedings of the National Academy of Sciences of the United States of America. 2004; 101:10780–10785. [PubMed: 15249687]

21. Shah VB, Aiken C. In vitro uncoating of HIV-1 cores. Journal of visualized experiments : JoVE. 2011; doi: 10.3791/3384

22. Warrilow D, Warren K, Harrich D. Strand transfer and elongation of HIV-1 reverse transcription is facilitated by cell factors in vitro. PloS one. 2010; 5:e13229. [PubMed: 20949087]

23. Cheley S, Gu LQ, Bayley H. Stochastic sensing of nanomolar inositol 1,4,5-trisphosphate with an engineered pore. Chemistry & biology. 2002; 9:829–838. [PubMed: 12144927]

24. Tanaka S, Sawaya MR, Yeates TO. Structure and mechanisms of a protein-based organelle in Escherichia coli. Science. 2010; 327:81–84. [PubMed: 20044574]

25. Chowdhury C, et al. Selective molecular transport through the protein shell of a bacterial microcompartment organelle. Proceedings of the National Academy of Sciences of the United States of America. 2015; 112:2990–2995. [PubMed: 25713376]

26. Kerfeld CA, et al. Protein structures forming the shell of primitive bacterial organelles. Science. 2005; 309:936–938. [PubMed: 16081736]

27. Price AJ, et al. Active site remodeling switches HIV specificity of antiretroviral TRIMCyp. Nature structural & molecular biology. 2009; 16:1036–1042.

28. Winn MD, et al. Overview of the CCP4 suite and current developments. Acta Crystallogr D. 2011; 67:235–242. [PubMed: 21460441]

29. Leslie AGW, Powell HR. Processing diffraction data with MOSFLM. Nato Sci Ser Ii Math. 2007; 245:41–51.

30. Evans PR. An introduction to data reduction: space-group determination, scaling and intensity statistics. Acta Crystallogr D. 2011; 67:282–292. [PubMed: 21460446]

31. Evans PR, Murshudov GN. How good are my data and what is the resolution? Acta Crystallogr D. 2013; 69:1204–1214. [PubMed: 23793146]

32. McCoy AJ, et al. Phaser crystallographic software. J Appl Crystallogr. 2007; 40:658–674. [PubMed: 19461840]

33. Murshudov GN, Vagin AA, Dodson EJ. Refinement of macromolecular structures by the maximum-likelihood method. Acta Crystallogr D. 1997; 53:240–255. [PubMed: 15299926]

34. Emsley P, Cowtan K. Coot: model-building tools for molecular graphics. Acta Crystallogr D. 2004; 60:2126–2132. [PubMed: 15572765]

35. Chen VB, et al. MolProbity: all-atom structure validation for macromolecular crystallography. Acta Crystallogr D. 2010; 66:12–21. [PubMed: 20057044]

36. Baker NA, Sept D, Joseph S, Holst MJ, McCammon JA. Electrostatics of nanosystems: Application to microtubules and the ribosome. Proceedings of the National Academy of Sciences of the United States of America. 2001; 98:10037–10041. [PubMed: 11517324]

37. Voss NR, Gerstein M. 3V: cavity, channel and cleft volume calculator and extractor. Nucleic Acids Res. 2010; 38:W555–W562. [PubMed: 20478824]

38. Zhao G, et al. Mature HIV-1 capsid structure by cryo-electron microscopy and all-atom molecular dynamics. Nature. 2013; 497:643–646. [PubMed: 23719463]

39. Gres AT, et al. X-ray crystal structures of native HIV-1 capsid protein reveal conformational variability. Science. 2015; 349:99–103. [PubMed: 26044298]

40. Julias JG, Ferris AL, Boyer PL, Hughes SH. Replication of phenotypically mixed human immunodeficiency virus type 1 virions containing catalytically active and catalytically inactive reverse transcriptase. Journal of virology. 2001; 75:6537–6546. [PubMed: 11413321]
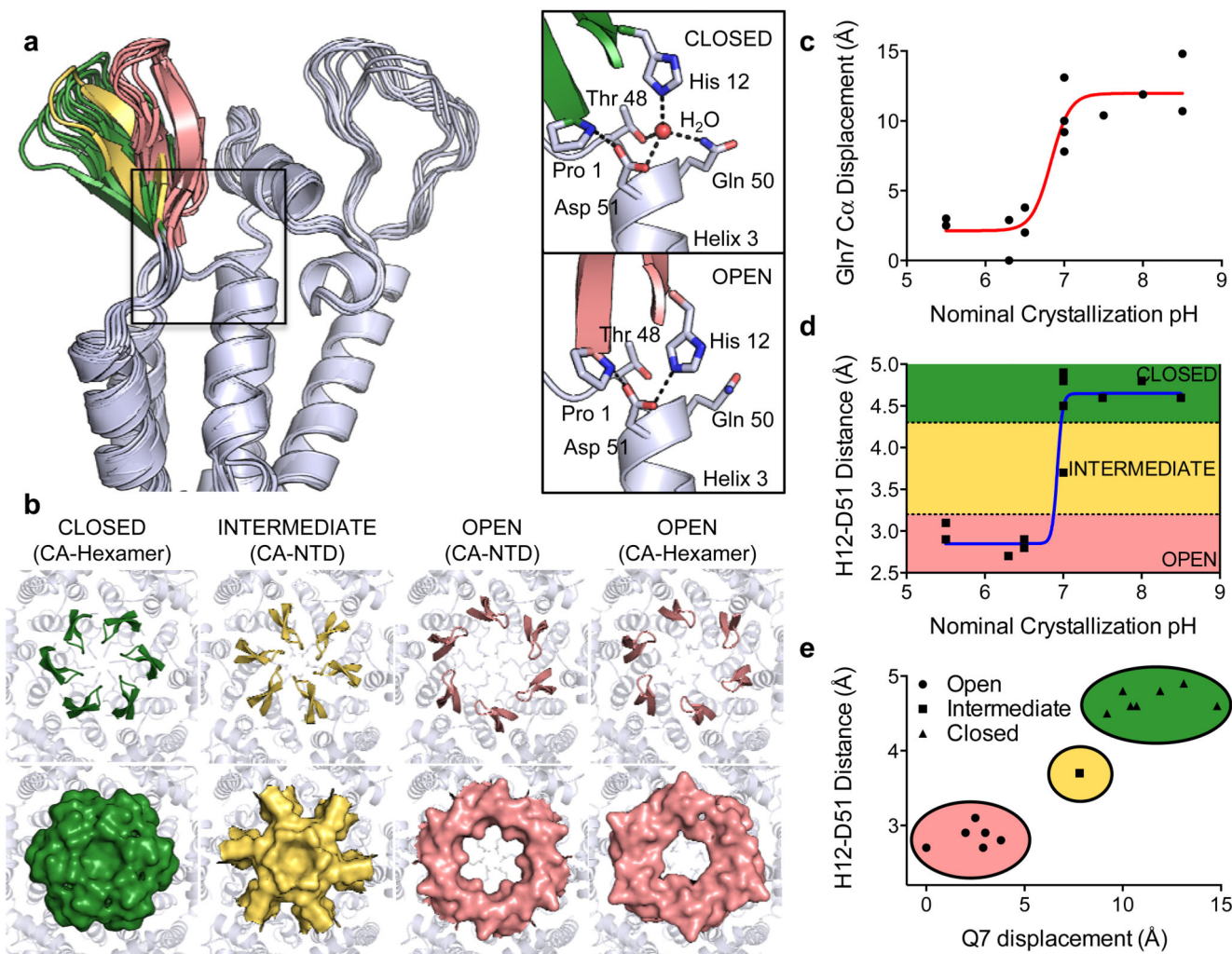
Figure 1. HIV-1 capsid hexamers have a pore at the 6-fold symmetry axis.
a, Superposition of N-terminal domains from solved capsid structures. A detailed view of the boxed region shows that the β-hairpin toggles between closed (green) and open (pink) states as a result of the hydrogen-bond network about P1, H12, and D51. **b,** β-hairpin (coloured) conformations dictate the presence of a pore at the 6-fold axis. Hexamers of CA N-terminal domain (CA-NTD) structures have been assembled using symmetry operators from $CA_{Hexamer}$ structures. **c,d** Displacement of Q7 or H12-D51 distance as a function of crystallization pH. **e,** Correlation of Q7 displacement with H12-D51 distance.
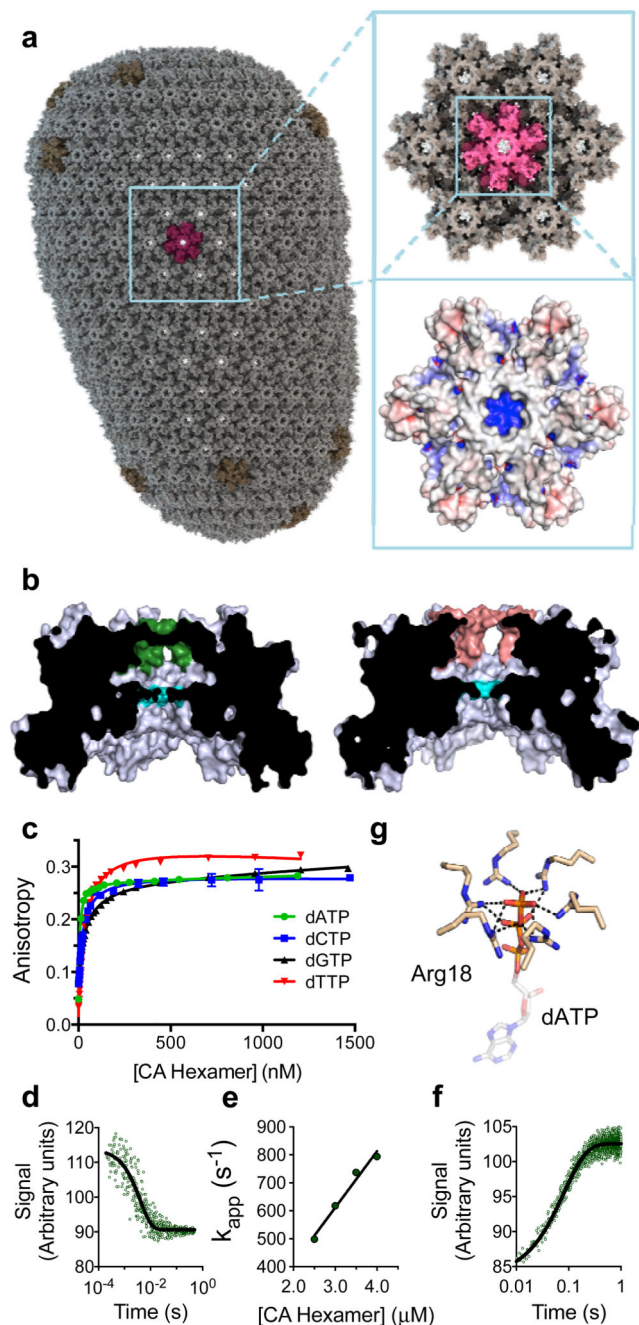
Figure 2. The HIV-1 capsid pore is strongly electropositive and recruits dNTP's with rapid association and dissociation kinetics.

a, Model of an HIV-1 virion with hexamers in an open conformation reveals that the capsid is porous. Surface electrostatic potential shows that the pores are highly electropositive. **b**, Cross sections through the closed (β-hairpin green) and open (β-hairpin pink) $CA_{Hexamer}$ showing a central chamber that is accessible in the open state. R18 (cyan) creates a bottleneck at the base of the chamber underneath the β-hairpin. **c**, Fluorescence anisotropy measurements of dNTP's binding to $CA_{Hexamer}$. **d**, Example of pre-steady state association

kinetics of dCTP with $CA_{Hexamer}$. **e**, Apparent rate constant (k_{app}) at increasing $CA_{Hexamer}$ concentrations. **f**, Dissociation of unlabeled dCTP:$CA_{Hexamer}$ by excess fluorescent-dCTP. **g**, R18 co-ordinates the phosphates in a dATP-bound $CA_{Hexamer}$ structure.
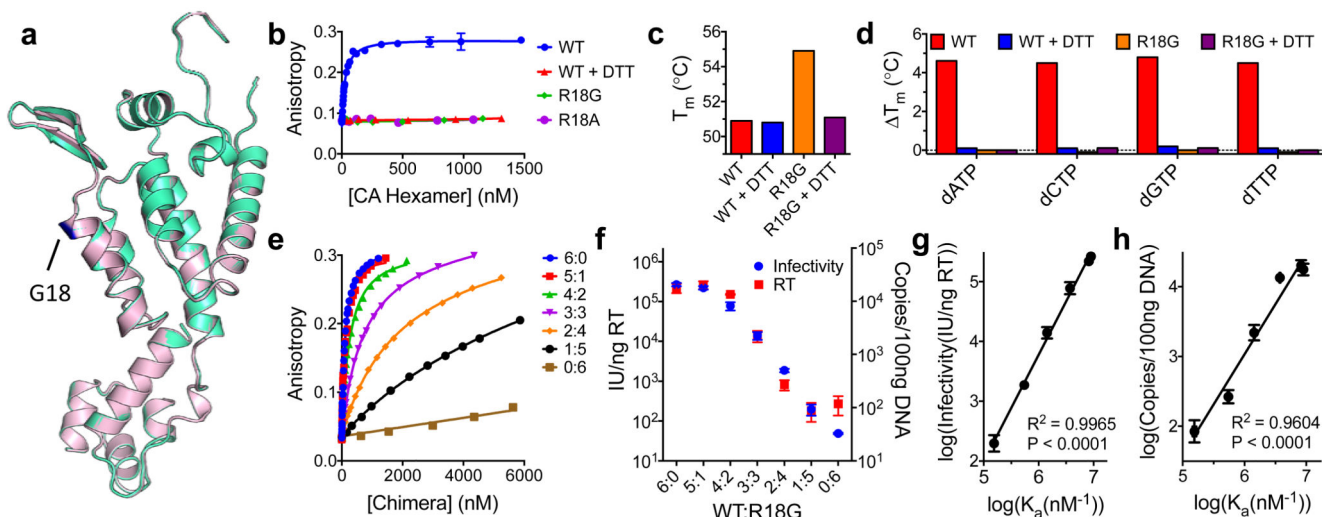
Figure 3. R18 is crucial for nucleotide recruitment, reverse transcription and infectivity.
a, Superposed monomers of R18G (light-pink) and wild-type (light-green) $CA_{Hexamer}$. **b**, Binding of capsid variants to dCTP as measured by fluorescence anisotropy. **c**, DSF stability measurements expressed as T_m for WT and R18G ± DTT. **d**, DSF measurements of the effect of dNTP's on the stability of WT and R18G expressed as T_m relative to unbound. **e**, Fluorescence anisotropy titrations of dTTP-binding by chimeric $CA_{Hexamers}$ with different R:G ratios at position 18. **f**, Comparison of infectivity and reverse transcription of chimeric viruses. **g,h**, Correlation between HIV-1 capsid dTTP affinity, viral infectivity **g** and reverse transcription **h**.
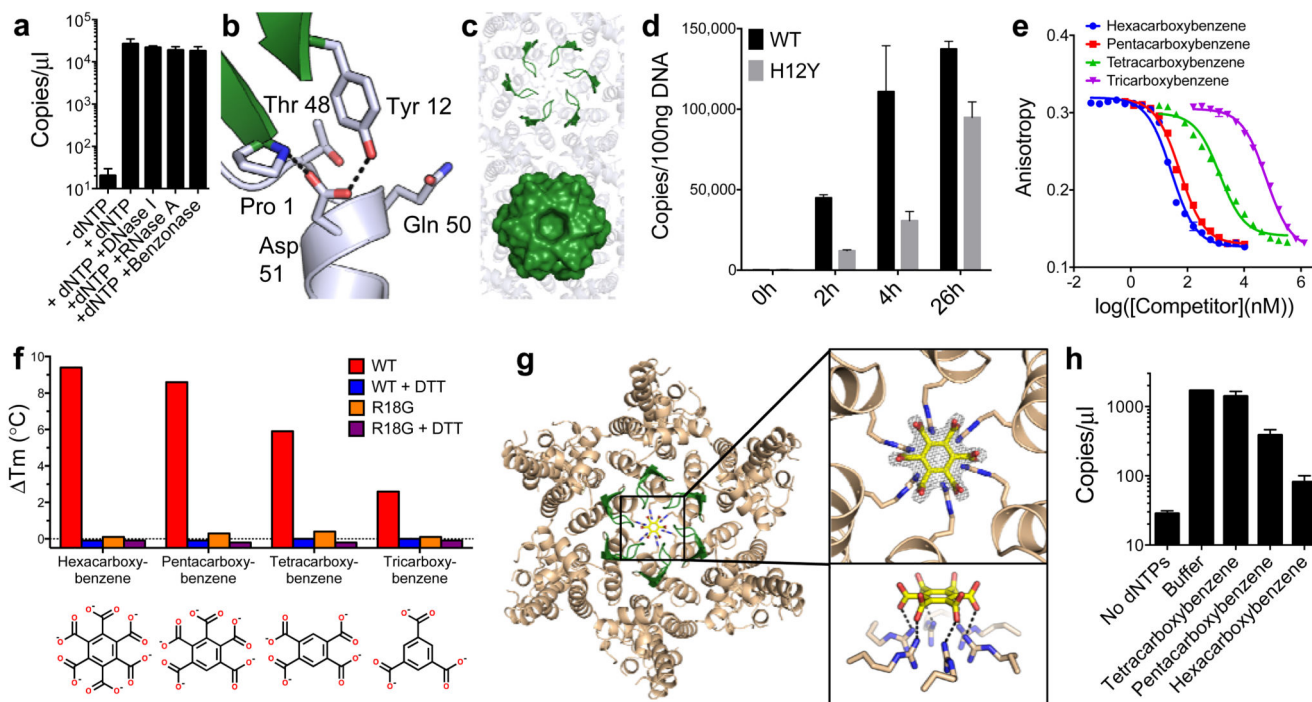
Figure 4. HIV-1 reverse transcription is inhibited by blockade of the capsid pore.
a, In vitro endogenous reverse transcription measuring strong-stop transcripts. **b**, Residues surrounding Y12 in the H12Y hexamer structure. **c**, Cartoon and surface representations of the β-hairpin in the H12Y hexamer. **d**, WT and H12Y reverse transcription kinetics. **e**, Competition binding of carboxybenzene compounds to $CA_{Hexamer}$. **f**, Change in wild type and R18G $CA_{Hexamer}$ T_m as measured by DSF in the presence of carboxybenzene compounds. **g**, $CA_{Hexamer}$ crystal structure in complex with hexacarboxybenzene, which is co-ordinated by R18. **h**, Effect of carboxybenzene compounds on endogenous reverse transcription.